SOFT ROBOTS

Bridging hard and soft: Mechanical metamaterials enable rigid torque transmission in soft robots

Molly Carton[1,2]*†, Jakub F. Kowalewski[3]*†, Jiani Guo[4], Jacob F. Alpert[3], Aman Garg[4], Daniel Revier[5], Jeffrey Ian Lipton[3]*

Torque and continuous rotation are fundamental methods of actuation and manipulation in rigid robots. Soft robot arms use soft materials and structures to mimic the passive compliance of biological arms that bend and extend. This use of compliance prevents soft arms from continuously transmitting and exerting torques to interact with their environment. Here, we show how relying on patterning structures instead of inherent material properties allows soft robotic arms to remain compliant while continuously transmitting torque to their environment. We demonstrate a soft robotic arm made from a pair of mechanical metamaterials that act as compliant constant-velocity joints. The joints are up to 52 times stiffer in torsion than bending and can bend up to 45°. This robot arm continuously transmits torque while remaining flexible in all other directions. The arm's mechanical design achieves high motion repeatability (0.4 millimeters and 0.1°) when tracking trajectories. We then trained a neural network to learn the inverse kinematics, enabling us to program the arm to complete tasks that are challenging for existing soft robots, such as installing light bulbs, fastening bolts, and turning valves. The arm's passive compliance makes it safe around humans and provides a source of mechanical intelligence, enabling it to adapt to misalignment when manipulating objects. This work will bridge the gap between hard and soft robotics with applications in human assistance, warehouse automation, and extreme environments.

INTRODUCTION

Soft robots leverage their distributed compliance to interact safely with humans (*1*) and the environment (*2*, *3*). However, entirely compliant robots struggle to twist objects and transmit continuous rotations. In applications such as reorienting parts in warehouse automation (*4*), fastening bolts during industrial assembly (*5*), or twisting multiturn valves in extreme human-engineered environments (*6*), soft robots remain unequipped to exert the necessary torque to manipulate their environment. For traditional robot arms, torque can be directly and continuously transmitted through links because of their torsional stiffness. Although this makes rigid robots efficient at twisting tasks, they carry inherent safety risks because of high mass and stiffness, resulting in robots working in structured environments isolated from humans. By mimicking soft biological appendages, such as elephant trunks (*1*, *7*–*10*) and octopus tentacles (*11*–*15*), soft robot arms are not only safe around humans but also can move with high dexterity and adapt to environmental uncertainty. Bioinspired robots that combine bending with extension gain additional agility over just bending (*16*, *17*). We need robot arms that combine the safety and dexterity of bending and extending with the utility of continuous torque transmission to work directly alongside humans.

Building soft robots from soft materials makes torque transmission inherently difficult. Materials such as elastomers are commonly used to build soft arms (*18*, *19*) but lack the torsional rigidity necessary for exerting torques. Existing flexible torque couplings, such as flex shafts and bellows, have notable limitations. Flex shafts have a high torsional rigidity and can be directly embedded within soft robots (*20*); however, they are only compliant in bending and, thus, restrict the robot from extending. Bellows, although able to bend and extend (*21*), are difficult to nest and must sacrifice their range of motion for torsional stiffness. Alternatively, twist actuation can be achieved by introducing chirality into a soft structure. Soft robots that use pneumatic artificial muscles with angled fibers (*22*, *23*), inflatable helical structures (*24*–*26*), vacuum-powered elastomeric twist actuators (*27*–*29*), foldable origami (*30*, *31*), and handed shearing auxetics (*32*, *33*) can transmit rotation, but all are confined to a finite range of motion. These existing solutions cannot be continuously driven to transmit multiple torques while remaining flexible in extension and bending.

Creating a soft robot arm that bends and extends but is torsionally stiff requires a material with both soft and hard modes of deformation. Specifically, we need a material that is much stiffer in twisting than in bending and extension. Biological structures, such as plants, have been observed to evolve large differences in torsional and flexural stiffness as a method of adapting to dynamic environmental conditions (*34*–*36*). By altering their morphometric parameters (axial and polar second moment of inertia), many species of plants use the geometry of their stems and petioles to control the relative stiffness of their deformation modes. Similarly, creating soft robots with a large stiffness differential between flexure and torsion can be done by tuning their elastic response at the geometric level. This is possible using mechanical metamaterials, where mechanical behavior is a function of both mesoscale geometry and material properties (*37*, *38*).

In this work, we present a robot made from a mechanical metamaterial that is stiff in torsion yet soft under all other deformation

[1]Department of Mechanical Engineering, Massachusetts Institute of Technology, 77 Massachusetts Ave., Cambridge, MA 02139, USA. [2]Department of Mechanical Engineering, University of Maryland, 4289 Campus Dr., College Park, MD 20742, USA. [3]Department of Mechanical and Industrial Engineering, Northeastern University, 390 Huntington Ave., Boston, MA 02115, USA. [4]Department of Mechanical Engineering, University of Washington, 3900 E Stevens Way NE, Seattle, WA 98195, USA. [5]Department of Computer Science, University of Washington, 185 E Stevens Way NE, Seattle, WA 98195, USA.
†These authors contributed equally to this work.
*Corresponding author. Email: mcarton@umd.edu (M.C.); kowalewski.j@northeastern.edu (J.F.K.); j.lipton@northeastern.edu (J.I.L.)

modes (Fig. 1 and Movie 1). We call these metamaterials torsionally rigid universal couplings (TRUNCs). A single coupling acts as a soft constant-velocity joint (fig. S2). Multiple couplings can be connected in series and parallel to create nestable flex shafts that transmit independent concentric torques along complex curves. We present an arm composed of these joints that can interface with common tools, such as socket drivers and wrenches, while remaining soft and safe around humans. By bending and extending similar to an elephant's trunk, the arm increases its workspace size and gains additional agility. Our cable-driven arm achieves high movement repeatability for trajectories (0.4 mm and 0.1°) that outperforms the current state of the art for soft multistage arms (*1*). Last, we demonstrate the real-world utility of our arm by having it install a lightbulb, assist a human with fastening bolts, and turn a shutoff valve. This work presents a robot arm that combines the safety and dexterity of soft robots with the utility of their rigid counterparts.

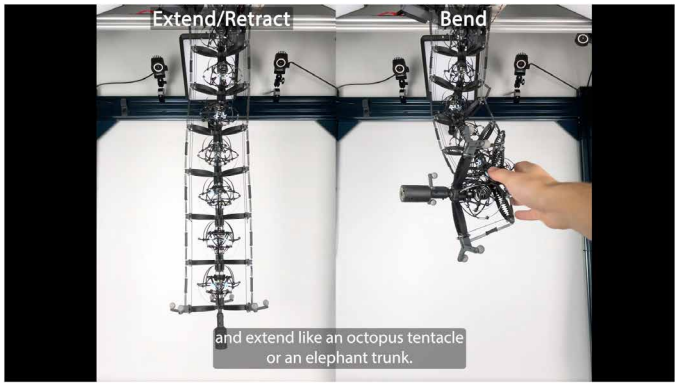

Movie 1. Motivation and summary of TRUNCs and the TRUNC arm.

RESULTS

Design and mechanical analysis

Flexible structures for continuous torque transmission should be nestable and focused on achieving a high torsional stiffness without reducing the overall range of motion. The primary existing solutions, bellows (*21*) and flex shafts (*20*), do not fully satisfy these performance metrics. Flex shafts are inextensible, and bellows trade off torsional rigidity with bending range of motion (see the Supplementary Materials). We, instead, took inspiration from metamaterial design to demonstrate a family of materials to build soft robots. We introduce point group auxetics to create TRUNCs.

Conventional auxetics are often modeled as, and constructed of, rigid links that connect at rotational joints. Auxetics expand along a trajectory controlled by a single phase angle γ that determines the expansion of the unit cell (identified for each cell with an arc in Fig. 2). As the phase angle increases, the cell expands in multiple directions up to a maximum phase angle γ_{max} (*32*). The symmetries of an auxetic are denoted here using orbifold notation. Orbifolds and their associated notation denote a symmetry group by its generating manifold (*39*).

The symmetry group building blocks for three-dimensional (3D) structures are the 3D point groups. The 3D point groups are those that preserve a point through a discrete set of translations and rotations, and, hence, they are also tilings of the surface of a sphere. They break down into two subsets, seven polyhedral groups and seven axial point groups. The axial point groups preserve a single axis of rotation. The preservation of an axis generates two poles and an equator and orients the structure. Although the polyhedral groups are finite, the axial groups form infinite families where the rotational and mirror symmetries around the axis can vary from two to infinity (*40*).

Because the axial point group structures have a pole and equator, they can have three basic rotational responses: The poles can twist relative to each other to produce a net twist, the equator can rotate relative to the poles, or there can be no relative rotation. The 2*N

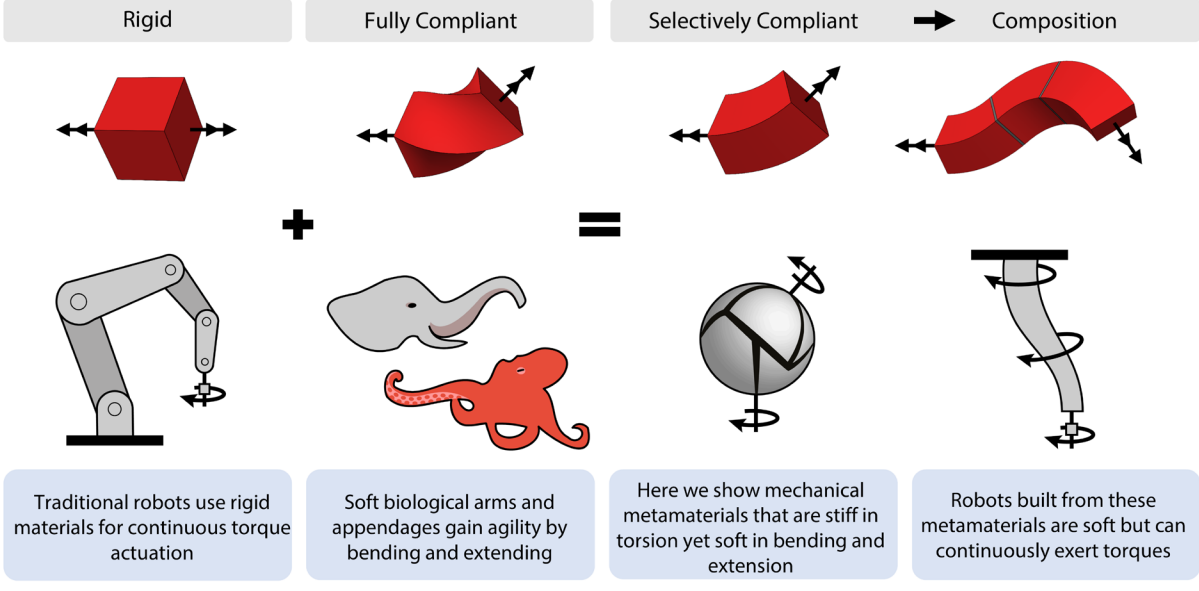

Fig. 1. TRUNC conceptual overview. We present a joint that is torsionally rigid yet compliant in bending and extension. The joint can be directly connected to a motor to create soft torque actuators. Multiple joints can then be composed to create soft arms with continuous torque actuation.

patterns, where N is any positive integer, maintain a structure along the equator of the sphere that connects to the poles, making them rigid to torsion.

We used these patterns to define a design space of TRUNCs, which encompasses their kinematic, geometric, and material parameters. The kinematic design space is defined by the tiling of a unit cell. The unit cell's geometry and properties are defined by the beam thickness and width (fig. S1A) relative to the neutral radius and the Young's modulus (E) of the base material. These, together, determine the mechanical performance of a TRUNC.

We designed TRUNCs as tilings of the auxetic double arrowhead structure seen in Fig. 2. Although there are N tilings of the cell around the equator defined by the symmetry group 2*N, there can also be M tilings between the poles, where M can be any number two or greater (fig. S1). As M increases beyond two, additional internal degrees of freedom are introduced. We therefore focused on two variations of the TRUNC joint that we call the equatorial ($M = 2$) and truss ($M = 3$) designs, shown in Fig. 2 (A and B), respectively.

Both variants behave as a spherical mechanism on a sphere of nonfixed radius and act as constant velocity joints (see the Supplementary Materials). The axial point group symmetry 2*N reduces the easy modes of deformation to extension or compression along the axis when unit elements are deformed axisymmetrically and bending along the axis is produced by an antisymmetric deformation of unit elements. Twisting along the axis is a stiff mode, allowing transmission of rotation along composed axes. We chose a fourfold equatorial symmetry, *4, because it is the simplest family that produces pairs of cells for expansion and compression in each direction. The internal mode of the truss structure ($M = 3$) allows shear internal to the cell, which can only be achieved through beam bending in the equatorial structure (Fig. 2, A and B). The result is cells that can extend, bend, and shear while being rigid to torsion.

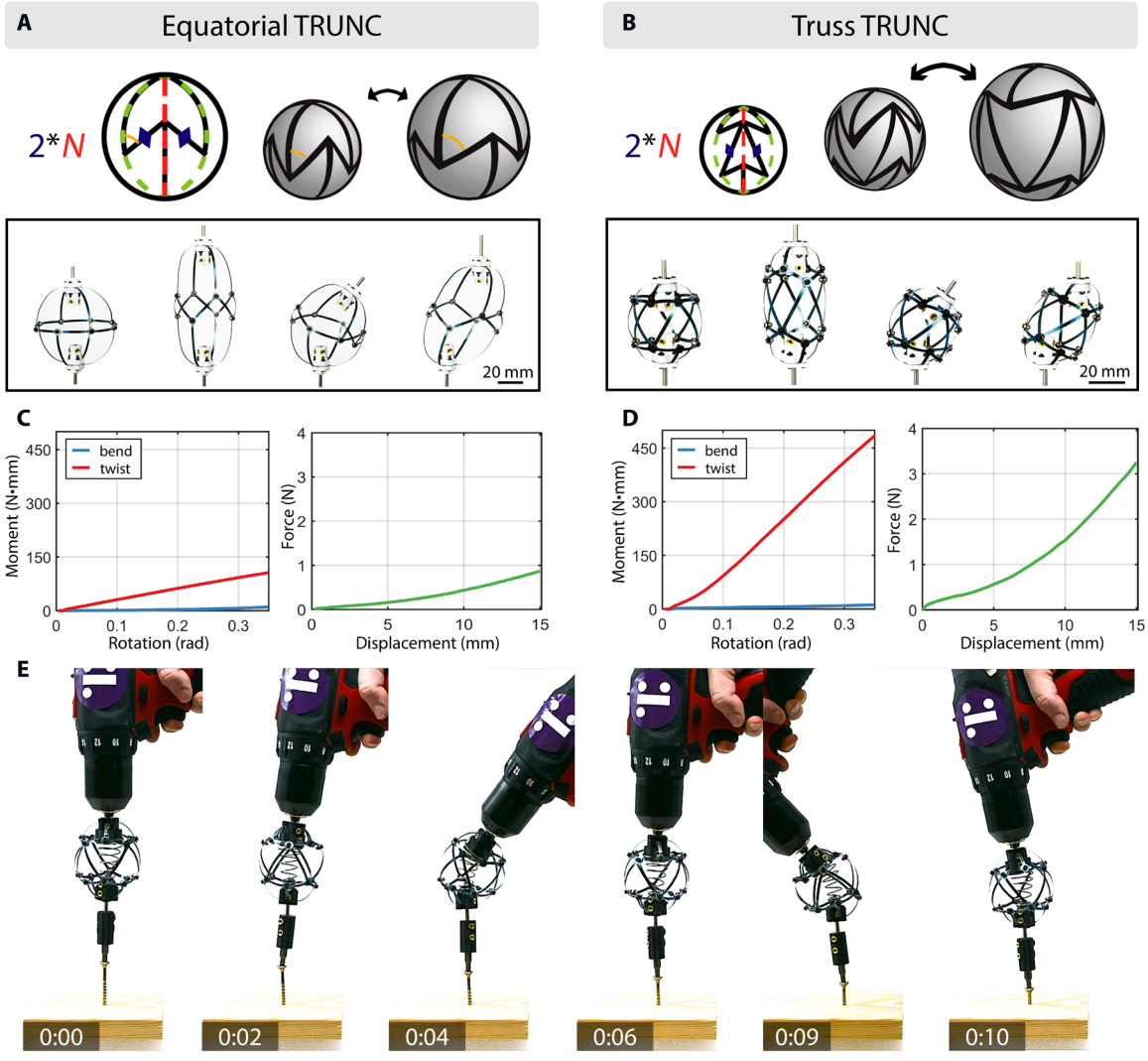

Fig. 2. The two TRUNC variants and mechanical properties. (**A**) The equatorial TRUNC has a single band of joints along its equator. Scale bar, 20 mm. (**B**) The truss TRUNC has two bands of joints on either side of the equator. This doubled structure allows for shear internal to the cell, which is disallowed in the equatorial structure. Scale bar, 20 mm. Moment rotation in twist and bending modes and force displacement in extension for the (**C**) equatorial cell and (**D**) truss cell demonstrate soft bending and extension compared with twist. (**E**) A truss TRUNC performing a screwing operation at various bend angles, demonstrating torque transmission while bending. An internal conical spring provides restoring force. A time stamp (minutes:seconds) is displayed in the bottom left corner of each frame.

We characterized the selective compliance of both TRUNC variants using the ratio of torsional stiffness to flexural stiffness. The twist-bend ratio can be expressed as GJ/EI using a specimen's E, shear modulus (G), axial second moment of area (I), and polar second moment of area (J). We note that the twist-bend ratio is the inverse of the ratio used to study plants, which often aim to minimize torsional stiffness and maximize flexural rigidity (*35*, *41*). We empirically characterized the flexural and torsional stiffness of both variants of the joints. The joints we characterized were made with spring steel (see Materials and Methods), and their stiffness values were found using linear regression on the moment-rotation data shown in Fig. 2 (C and D). Our results show that both variants are substantially stiffer in twisting than in bending. The equatorial TRUNC (Fig. 2A) has a twist-bend ratio of 11, and the truss variant (Fig. 2B) has a ratio of 52. In simulation, we investigated the fabrication design space parameters, defined by the material choice, cell diameter, and link width and thickness. We found that although the twist-bend ratio of both cells increased with a material's elastic modulus, the truss cell was less sensitive to changes between stiff materials (fig. S3). Furthermore, as the link's width and height increased relative to the cell's diameter, the twist-bend ratio increased and the performance gap between both cell variants became smaller (see the Supplementary Materials).

Given their large twist-bend ratios, TRUNCs can serve as highly flexible torque couplings. They can bend up to 45° from the neutral state while remaining 85.7% efficient in torque and energy transmission (fig. S6A). This gives them the flexibility of rubber bellows while remaining much closer to the torsional rigidity of steel bellows, which can only bend up to 10°. To illustrate the TRUNC's torsional rigidity, we connected a truss joint to a power drill and drove a screw into birch wood at various bend angles (Fig. 2G and movie S1). A conical spring was added inside the cell to provide a restoring force without transmitting any torsional load because its rotational degree of freedom is not rigidly constrained. This demonstrates how the TRUNC's large twist-bend ratio enables torque transmission through the hard mode while accommodating misalignment through the soft modes. To demonstrate the fatigue resistance of the cells, we cycled seven cells through more than 6800 cycles with strains of more than 10% without failure (see the Supplementary Materials).

TRUNCs can be chained and nested

The two TRUNC variants we previously introduced can be composed into larger metamaterials by connecting them in series or by concentrically nesting them as shown in Fig. 3. When connected in series, fixed axis to axis, the TRUNCs act as a flexible shaft, conveying rotational motion and torque along a curved path. We show how a TRUNC made as a continuous material with living hinges can deform and transmit rotation. However, unlike traditional flex shafts, our design is extendable. When stretched by 20% of its length, the TRUNC flex shaft maintained 83.6% of its original torsional rigidity (Fig. 3B). Chained TRUNCs can mimic the extension of elephant trunks while maintaining their stiff torsional coupling properties.

To transmit multiple concentric torques, flexible torque couplings should nest efficiently inside each other. Because TRUNCs are based on spherical geometry, they can easily be nested as a series of concentric shells with ample room for clearance. This concentric composition is limited only by space and can theoretically provide an infinite number of rotational degrees of freedom. Nested TRUNCs bend and extend in unison but rotate independently (Fig. 3D). TRUNCs can be nested much more efficiently than bellows because more than 85% of their volume is unoccupied, compared with 35% or less in bellows couplings (see the Supplementary Materials). When nested, a small cross-coupling effect exists between the cells because of friction within the bearings of the assembly (fig. S3). This allows nested TRUNCs to transmit multiple independent torques through the same bend angle.

When cells were nested and chained (Fig. 3E), they created a flex shaft that can transmit multiple torques independently along its length. To demonstrate this, we connected the flex shaft to a rotational gauge with two indicator dials. We then independently controlled the dials by switching the input torque between the inner and outer columns of the flex shaft (see Fig. 3 and movie S2). When the inner shaft was driven, the green dial moved, and the red remained still even as the arm deformed. When the outer shell was driven, the inner green dial remained still. This demonstrates that the drill was only weakly connected to the dial indicator in terms of position, although the torsional connection remained strong. This allows us to build couplings that move freely through space while transmitting an arbitrary number of independent torques. Moving beyond soft materials to mechanical metamaterials enables us to build torque transmissions that rigidly couple input and output drives while remaining flexible in bending and extension.

A soft robotic arm composed of TRUNCs

The nested TRUNC flex shafts we showed in the previous section enabled us to create soft robots capable of continuous torque actuation. Our arm's design rigidly coupled the end effector to a drill motor statically mounted at the base using a truss flex shaft. This layout leverages the benefits of direct motor drives while maintaining the robot's low inertia. The truss flex shaft was then nested within an equatorial shaft that guided the actuation tendons that control the arm (Fig. 4A). The cable actuation system used nine servo motors mounted at the base. The nine cable lengths define the arm's configuration space $\mathscr{L} \in \mathbb{R}^9$ and encode all possible arm poses. Cables attach to the arm at three active joints that we call the shoulder, elbow, and wrist. The remaining joints connected between are passive. In its neutral state $\mathscr{L}_{\text{home}}$, the arm's cables were minimally pretensioned to a manually configured set point. An active joint could then be bent and compressed by varying the three corresponding cable lengths. This deformation was coupled to the passive joints above the active joint, allowing smooth bending and compression along each arm segment. We used springs to provide restoring forces that extend the arm as cable tension is released. The cables attached to the arm using spring structures that bend and twist in-plane, allowing them to remain compliant to contact forces (Fig. 4C) but resist out-of-plane bending when actuated. Our arm design combines the advantages of soft bioinspired arms with the utility of direct and continuous torque actuation.

Bending and extension enable the arm to position the end effector within a sizable workspace. We empirically measured the arm's reachable workspace by recording the end effector's position over a bounded subspace of $\mathscr{L}$ consisting of 18,300 poses (see Materials and Methods). The boundaries of this subspace were found experimentally by driving the arm to extremal poses. The workspace was then reconstructed by fitting an alpha shape ($\alpha = 34.4$ mm) to the 3D point cloud, producing a concave hull with a volume of 18,272 cm^3 (Fig. 4D). The projection of the workspace onto the xy

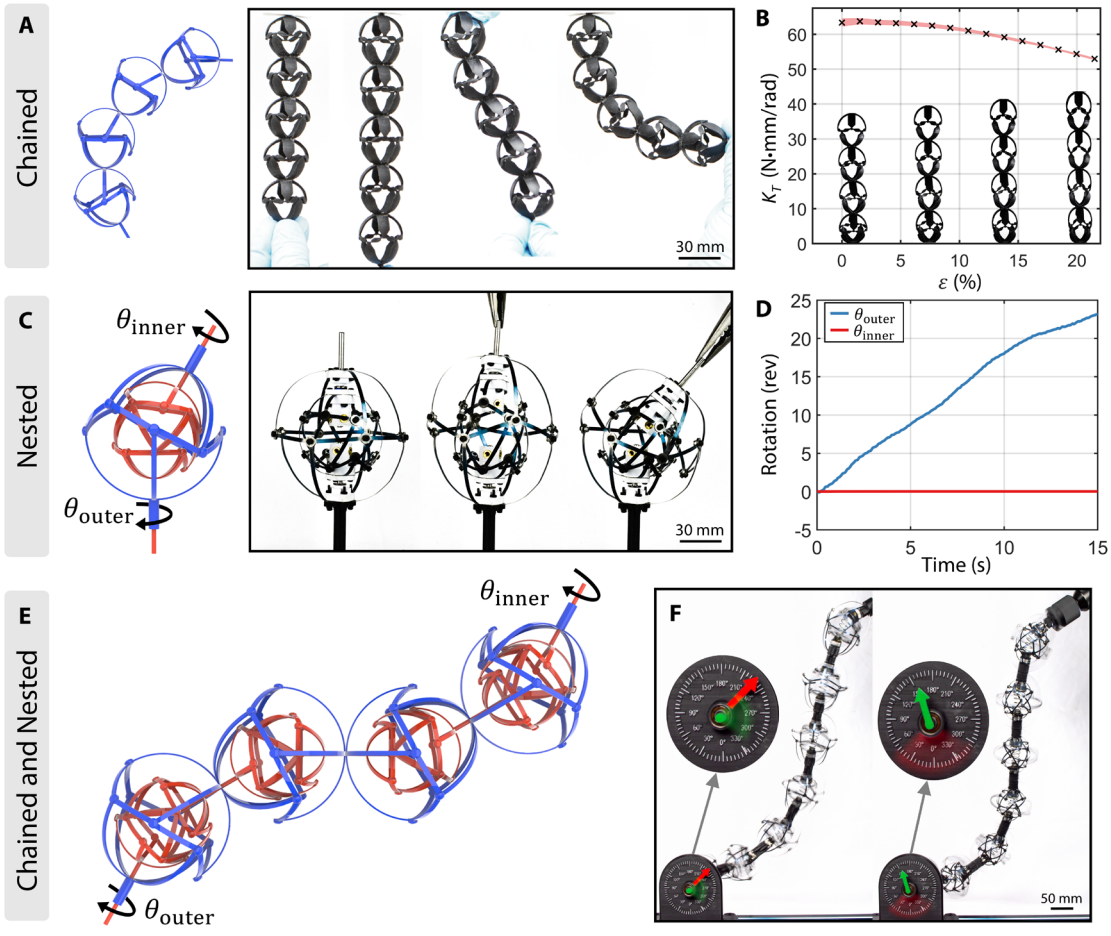

Fig. 3. Composition of TRUNCs. (**A**) Joints can be chained in series to create flex shafts that transmit torque while bending and extending. Scale bar, 30 mm. (**B**) TRUNC flex shafts remain torsional rigid under extension. The red boundary represents the minimum and maximum bounds of the torsional stiffness K_T for $n = 5$ trials. (**C**) Joints can also be concentrically nested. Scale bar, 30 mm. Nested joints are coupled in bending and extension but (**D**) rotate independently. (**E**) Nested joints can be chained to create flex shafts that transmit multiple torques. (**F**) Each column of the flex shaft rotates separately, allowing multiple independent rotational degrees of freedom. Scale bar, 50 mm.

plane approximated a circle with a diameter of 600 mm or 84.5% of the arm's neutral length ($l = 710$ mm). The cross-sectional view of the *xz* projection shows that the workspace is symmetric about the *z* axis and illustrates how the extension degree of freedom increases the total volume. We note that the workspace is thickest near the origin and becomes thinner near the edges. This thinning effect occurs because the arm undergoes additional compression while bending, which reduces its range of motion. From our workspace analysis, we found that the arm can compress up to $\Delta l = 94.3$ mm, or 13.3% of its length in the *z* direction, and tilt the end effector up to 83.9° from the ground plane.

Within this recorded workspace, we characterized the positional and angular repeatability of the arm's movements. Because of nonlinear and hysteretic effects, a soft robot's state at any time is influenced by its history of previous states (*42*). Thus, we used separate tests to measure repeatability for point positioning and trajectory following. We generated the test trajectory by randomly selecting 100 configurations and ordering them using *K*-nearest neighbors as a greedy solution to the traveling salesman problem. The point repeatability test used the same points but randomized the order at the start of each trial. Before each trial, the arm cycled five times between its neutral and fully compressed state to reset any hysteretic effects from previous tests. For each test, the arm visited the 100 points over five trials, and we calculated the translational and angular distance of each data point from its cluster's mean. For point positioning, we found the SD of the residual distances to be 2.1 mm and 0.1° (Fig. 4E). When tracking a trajectory, the SD decreased to 0.4 mm and 0.1° (Fig. 4F). With millimeter-level trajectory repeatability, our arm outperforms state-of-the-art multistage soft arms on trajectory precision (*1*).

Experimental demonstration

Continuous torque actuation can enable soft robots to perform a broader range of real-world tasks than their completely compliant counterparts. We trained a neural network to learn the arm's inverse kinematics (see Materials and Methods) and demonstrated the TRUNC arm installing a light bulb, fastening bolts for a motherboard, and shutting off a valve. For these experiments, we measured the position of target objects (see Materials and Methods) and then used the learned inverse kinematics model to generate each

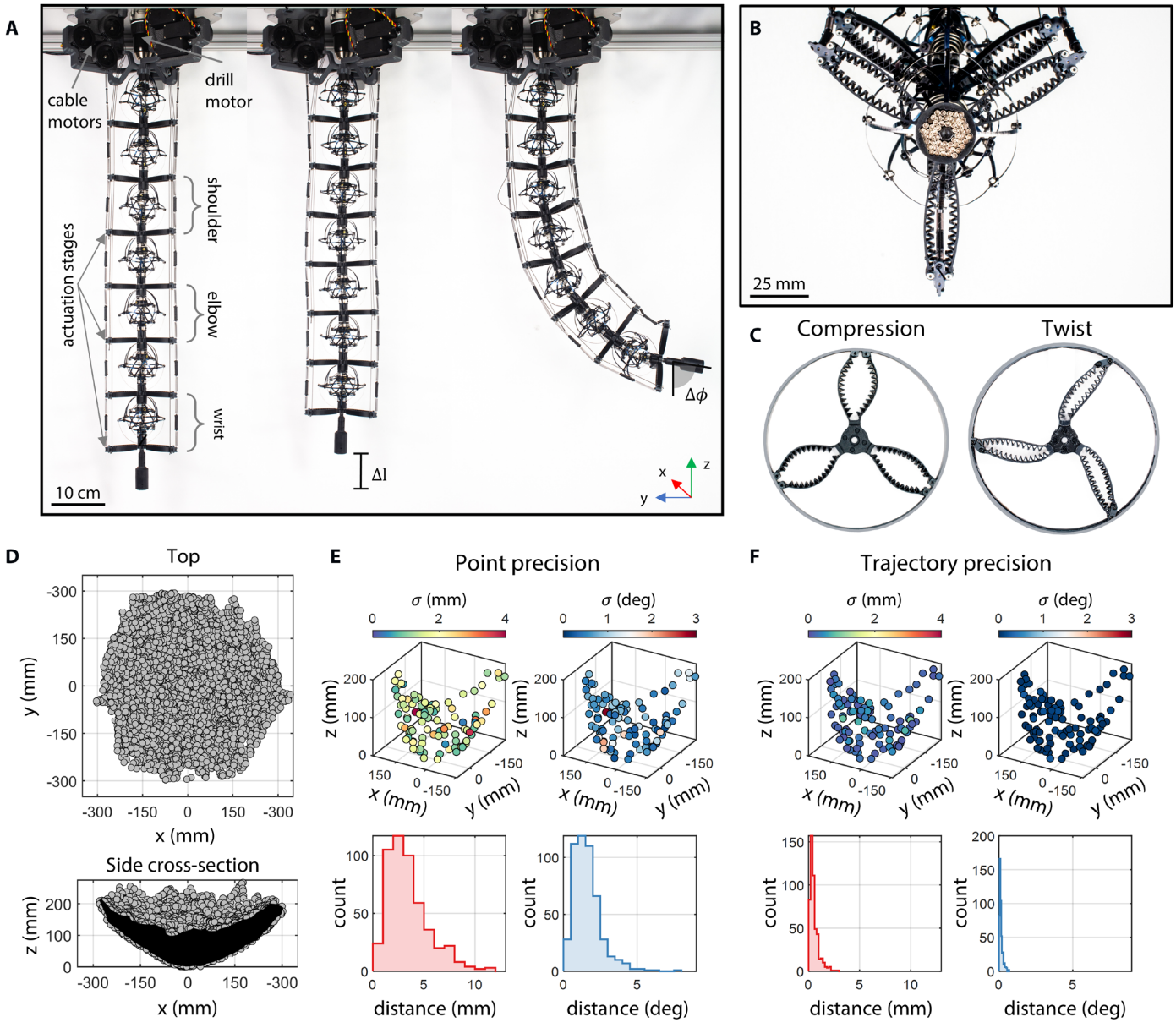

Fig. 4. Design and analysis of the TRUNC arm. (**A**) The body of the robotic arm consists of two nested flex shafts. Torque is transmitted to the end effector using a drill motor mounted at the base. Scale bar, 10 cm. (**B**) A head-on view of the arm with the socket driver end effector. Scale bar, 25 mm. (**C**) The cables are connected via a structure that can bend and twist in plane but resists out-of-plane bending. (**D**) The workspace was empirically measured by sampling 18,300 poses. The bounding hull is concave and approximately symmetric about the *z* axis. A cross-sectional view shows how the arm increases its workspace volume by extending along its length. (**E**) The arm's positional and angular repeatability when visiting points in a random order (point precision) and (**F**) a fixed order (trajectory precision). Plotted points represent averaged values across $n = 5$ trials, and the color map is the SD.

trajectory. In the first experimental demonstration, the arm installed a light bulb into a lamp (Fig. 5A and movie S3). Our end effector was a commercially available universal light bulb changer that grips the bulb using rubber-coated steel. The arm first positioned the bulb above the socket before lowering it into place. Compliance enabled the arm to passively align itself for peg-in-hole insertion tasks. The arm leveraged this by extending past the targeted *z* height to increase the insertion force, helping the bulb's threads engage once the bulb started rotating. Once positioned within the socket, the bulb was rotated by 2½ revolutions, which completed the circuit and turned it on. The arm then disengaged with the bulb by pulling the end effector up before returning to the home position. This demonstrates that even using simple motion planning, the arm could carefully handle and manipulate delicate objects and perform complex fastening operations.

In the next experiment, we used the TRUNC arm to work alongside a human and install a motherboard on a mounting frame (Fig. 5B and movie S4). The assembly began with the human placing the board on the standoffs and prefastening the M6 bolts by two turns each while the arm waited nearby. Once the board was placed, the

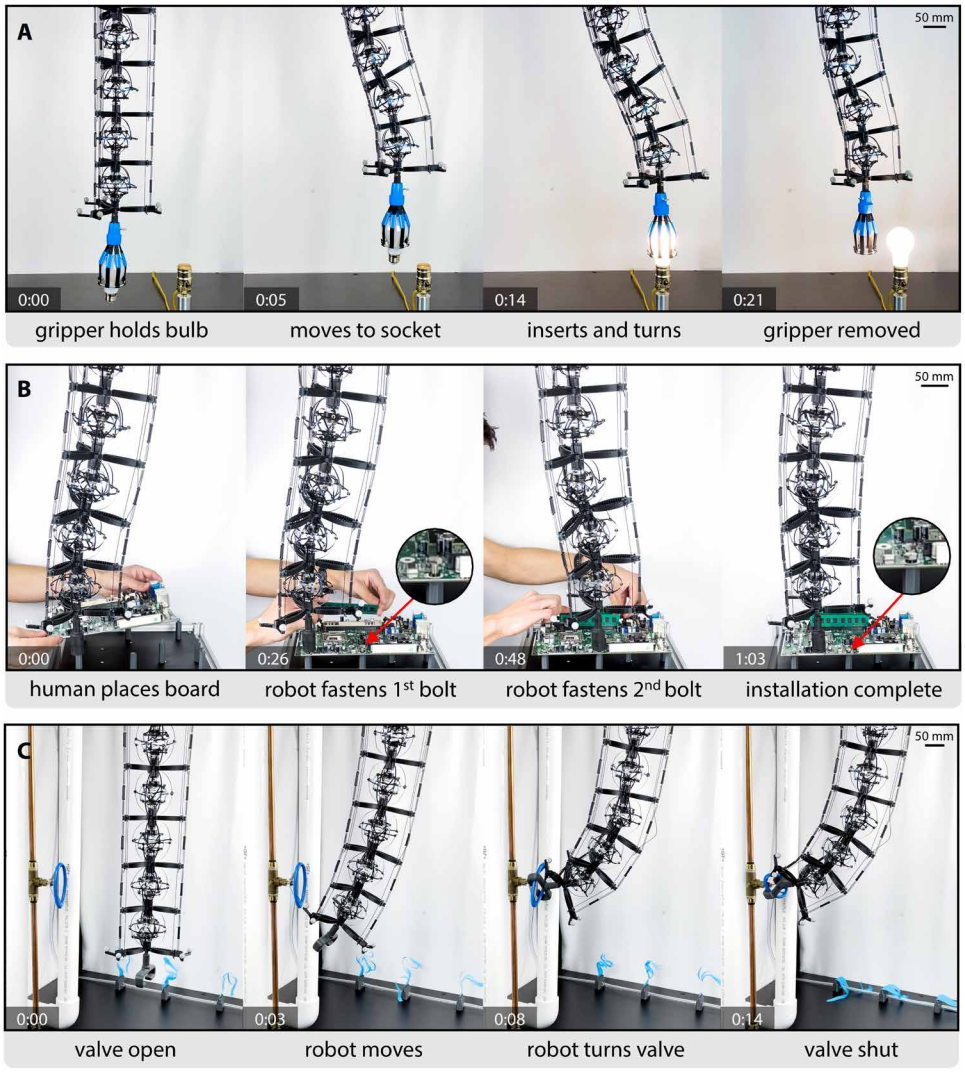

Fig. 5. Demonstrating applications for the TRUNC arm. (**A**) Delicately installing a light bulb into a lamp. The arm positioned the bulb and then rotated it until the bulb turned on. Scale bar, 50 mm. (**B**) Safe human-robot collaboration for motherboard installation. The robot secured the board to the frame by fastening bolts, while the human installed computer memory modules. Scale bar, 50 mm. (**C**) Manipulating a valve positioned between two plastic pipes to shut off airflow. Scale bar, 50 mm. A time stamp (minutes:seconds) is displayed in the bottom left corner of each frame.

arm received a command to begin fastening bolts that secured the board to an aluminum frame. As the arm fastened bolts, the human worked alongside it by installing computer memory modules. The arm was programmed to position the socket above each fastener before lowering in the $-z$ direction. The end effector's universal socket adapter (Fig. 4B) had spring-loaded pins that decouple the need for simultaneous extension and rotation during thread fastening operations. This enabled the arm to hold its position while transmitting torque to fasten each bolt by 7¾ revolutions. Automating this thread-fastening subroutine allowed the human co-worker to continue working safely in parallel with the robot.

Last, we showed how the arm can manipulate objects within constrained spaces. This demonstration simulated a leak scenario where the arm had to reach and turn a valve positioned between two pipes (Fig. 5C and movie S5). We used a 3D-printed wrench end effector that passively gripped and locked onto the valve once it began turning. The arm's continuous end effector rotation simplified the task because the gripper did not need to disengage and reengage while operating in a tight space. The arm combined bending with linear translation to reach the valve and slide the end effector over it. A smooth motion transition in orientation was achieved using spherical linear interpolation between the home and target quaternions. Once engaged with the valve, the arm applied 3½ clockwise rotations, which successfully shut off airflow as indicated by the outlet's blue streamers. While actuating the valve, the arm passively deformed to compensate for misalignment between the wrench and valve's center of rotation.

DISCUSSION

We present the TRUNC arm, a flexible soft robot that has the utility of continuous torque actuation. The arm's design was based on a pair of soft extendable constant-velocity joints capable of continuous torque actuation. We introduced and characterized two variants of the joint based on the same symmetry group. The joints achieved a wide range of motion in compression and bending. The selective compliance built into their design, with a low axial and bending stiffness but high torsional rigidity, allows TRUNCs to be coupled with motors to create soft actuators that can transmit torque.

We showed how composing TRUNCs enables them to transmit multiple torques over longer distances. The first composition method connected joints in series to create flexible shafts capable of bending and extending, whereas nesting joints inside each other enabled concentric torque transmission. We combined both methods to create a nested flex shaft with two rotational degrees of freedom about the central axis that we independently actuated in Fig. 3E.

We applied these principles to create a soft arm with continuous torque actuation. The cable-driven arm transmitted torque to its end effector using a flexible TRUNC shaft connected to a motor mounted at its base. We demonstrated that the arm could compress up to 13.3% of its length and tilt the end effector up to 83.9° from the ground plane. The arm could position the end effector within a large workspace by bending, compressing, and extending and moved with high motion repeatability along trajectories (0.4 mm and 0.1°). This enabled the arm to perform many real-world tasks that were previously inaccessible to soft robots.

We chose three tasks to demonstrate the versatility of the TRUNC arm using different end effectors in different environments. The first

task, installing a light bulb, demonstrated that the arm has the mobility to extend and twist while manipulating delicate objects and to passively align itself when fastening threads. In the second task, the arm worked safely around a human to install electronic components. In the third task, the soft arm was able to navigate a close environment to shut off a valve by rotating it continuously over multiple turns. Using selective compliance, the arm combined flexibility with robust manipulation. This work bridges the gap between soft and rigid robots by combining the safety of compliant structures with the utility of rigid and continuous torque transmission.

MATERIALS AND METHODS

Cell and arm fabrication

The monolithic flexure TRUNCs were printed on a Carbon M1 printer using FPU 50 resin. Spring steel TRUNCs were assembled from laser-cut 0.01-inch (0.254-mm) 1095 hardened spring steel. Technical drawings are provided in the Supplementary Materials. Spring steel parts were sanded around the joint locations to expose the bare metal, removing defects, burs, and surface coatings. Steel links were manually bent using a 56-mm-diameter spherical mold for the truss cells and an 88-mm-diameter mold for equatorial cells. The links were then assembled using M2 screws and nylon lock nuts. Chained cells were connected using a 4-mm steel rod press-fit into a bearing (McMaster part ID: 6655K47) that was fastened to the cell with a 3D-printed connector. Heat-set threaded inserts were installed to fix the coupling shafts to the cells. Nesting cells were offset with a thrust bearing (McMaster part ID: 6655K47) between the contacting surfaces to reduce friction.

We used nine Hitec HS-785HB winch servos for the cable actuation system. The home configuration ($\mathscr{L}_{\text{home}}$) was found during the arm's setup by controlling each motor until its cable's slack was removed. The cable attachment triads (Fig. 4C) were fabricated on a Prusa MK4 extrusion 3D printer in PLA+. The triad structures route the cables through an embedded polytetrafluoroethylene lining to reduce friction. Actuating cables were 0.75-mm synthetic braided cables. A conical spring (K = 1.22 N/mm) was mounted inside each cell with a free length longer than the inner sphere diameter so that the cells were pretensioned, providing a restoring force for the arm. The arm also had six extension springs (K = 0.07 N/mm) for each cell that provided restorative forces when bending. Torque was transmitted to the end effector using an 18-V dc Milwaukee drill motor (connected to a 2.15-V power supply) and was toggled using a relay module. The motors and arm were mounted to a 0.25-inch (6.35-mm) aluminum base plate that was fixtured to the motion capture booth.

Kinematic characterization using rotational encoders

Kinematic tests for the joints (Fig. 3D and fig. S2) were conducted using two YUMO E6B2-CWZ3E rotational encoders connected to a National Instruments USB-6009 data acquisition unit. The input and output shafts were connected to separate encoders mounted on a steel fixture plate, and a 12-V dc motor was then used to drive the input shaft. Data were sampled at a rate of 10,000 Hz, and the quadrature signals were read and decoded in MATLAB.

Mechanical characterization

The tensile, torsional, and flexural tests were performed using an Instron CCP122055 biaxial load cell (±450 N and ±5 N·m). For the spring steel TRUNCs, we applied WD-40 to the spring to reduce friction. In our bending and torsion tests, we rotated the cell by −5° before returning to the origin to reduce backlash effects. Data were collected at intervals of 1° with an angular velocity of 1 rpm. In our extension tests, we precompressed the cell to −2 mm before returning to the origin. Data were then collected at intervals of 0.2 mm with a linear velocity of 0.5 mm/s.

Motion capture setup

We captured the ground truth pose of the arm using an OptiTrack motion capture system with eight Flex 13 cameras and streamed the data to MATLAB using NatNet. The workspace dataset (Fig. 4D) and trajectory tests (fig. S9) tracked the end effector using the socket tool with four markers affixed at the base. Because the inverse model was trained on data collected with the socket end effector, we measured a coordinate transformation for each tool to compensate for geometric differences when generating new trajectories. For our experimental demos (Fig. 5), we measured the position of the target objects (bolts, socket, and valve) using 3D-printed mounts for motion capture markers before testing.

Neural network training

We trained our inverse kinematic model on the workspace dataset (Fig. 4D), consisting of 18,300 pairs of configuration states and end effector poses. Randomly sampling the configuration space of cable-driven poses resulted in ill-defined configurations where the arm lost actuation degrees of freedom because of slack or "dead bands" in the cables. Our learning approach sampled $\mathscr{L}$ using an approximate kinematic model (see the Supplementary Materials) and refined these configurations during the data collection process by slowly tensioning each cable until the end effector moved by more than 3 mm or 1°. In addition, we enforced a bijective mapping to SE(3) by virtually coupling the shoulder and elbow rotations (see the Supplementary Materials). The dataset was normalized using minimum-maximum normalization and then split into training (80%) and validation (20%) sets.

The deep neural network was implemented in PyTorch and consisted of three fully connected layers. The input layer size (seven neurons) corresponded to the end effector's position (x, y, z) and orientation represented as a quaternion (q_w, q_x, q_y, q_z). There were two hidden layers with 1600 neurons each and rectified linear unit activation functions to introduce nonlinearity. Last, the output layer had nine neurons corresponding to the dimensions of $\mathscr{L}$. For our loss function, we used the mean squared error between the predicted and actual arm configurations. When training, we used the Adam optimizer with a learning rate of 0.001, a momentum of 0.9, and no weight decay. The learning rate was annealed using exponential decay with $\lambda = 0.9$. We used a batch size of 16 to balance computational efficiency and the granularity of learning. The model was trained for 50 epochs, which took 120.6 s using a cloud-based graphics processing unit (Nvidia Tesla v100). The final mean training error was 1.04 mm per cable, whereas the mean validation error was 1.11 mm per cable. When performing inference to generate trajectories, the model was run on the computer's central processing unit (12th-generation Intel i7-12700 2.10 GHz) and took on average 0.368 ms per waypoint. Trajectory-following results are provided in the Supplementary Materials.

Statistical analysis

When quantifying uncertainty for empirical results (Fig. 3B and figs. S5, B and C, and S7), we performed $n = 5$ consecutive trials and averaged the results. We then defined our uncertainty bounds as the minimum and maximum values at each sampled interval. For the TRUNC arm repeatability tests in Fig. 4 (A and B), we also performed $n = 5$ trials but quantified uncertainty using the SD to ensure consistency with established performance metrics for soft arms (*1*).

Supplementary Materials

The PDF file includes:
Materials and Methods
Figs. S1 to S9
Legends for movies S1 to S5

Other Supplementary Material for this manuscript includes the following:
Movies S1 to S5

REFERENCES AND NOTES

1. Q. Guan, F. Stella, C. Della Santina, J. Leng, J. Hughes, Trimmed helicoids: An architectured soft structure yielding soft robots with high precision, large workspace, and compliant interactions. *NPJ Robot.* **1**, 1–13 (2023).
2. E. Del Dottore, A. Mondini, N. Rowe, B. Mazzolai, A growing soft robot with climbing plant-inspired adaptive behaviors for navigation in unstructured environments. *Sci. Robot.* **9**, eadi5908 (2024).
3. E. W. Hawkes, L. H. Blumenschein, J. D. Greer, A. M. Okamura, A soft robot that navigates its environment through growth. *Sci. Robot.* **2**, eaan3028 (2017).
4. N. Correll, K. E. Bekris, D. Berenson, O. Brock, A. Causo, K. Hauser, K. Okada, A. Rodriguez, J. M. Romano, P. R. Wurman, Analysis and observations from the first Amazon picking challenge. *IEEE Trans. Autom. Sci. Eng.* **15**, 172–188 (2016).
5. S. Hamdule, S. S. Goilkar, "An overview of the untapped potential of soft robotic arms with integration of machining tools" in *Machining and Additive Manufacturing* (Springer Nature, 2024), pp. 107–115.
6. E. Krotkov, D. Hackett, L. Jackel, M. Perschbacher, J. Pippine, J. Strauss, G. Pratt, C. Orlowski, in *The DARPA Robotics Challenge Finals: Humanoid Robots To The Rescue*, M. Spenko, S. Buerger, K. Iagnemma, Eds. (Springer International Publishing, 2018), pp. 1–26.
7. M. W. Hannan, I. D. Walker, Kinematics and the implementation of an elephant's trunk manipulator and other continuum style robots. *J. Robot. Syst.* **20**, 45–63 (2003).
8. A. Grzesiak, R. Becker, A. Verl, The bionic handling assistant: A success story of additive manufacturing. *Assem. Autom.* **31**, 329–333 (2011).
9. Q. Guan, J. Sun, Y. Liu, N. M. Wereley, J. Leng, Novel bending and helical extensile/contractile pneumatic artificial muscles inspired by elephant trunk. *Soft Robot.* **7**, 597–614 (2020).
10. A. Zhang, T.-H. Wang, R. L. Truby, L. Chin, D. Rus, Machine learning best practices for soft robot proprioception, in *2023 IEEE/RSJ International Conference on Intelligent Robots and Systems (IROS)* (IEEE, 2023), pp. 2564–2571.
11. G. Immega, K. Antonelli, The KSI tentacle manipulator, in *Proceedings of 1995 IEEE International Conference on Robotics and Automation* (IEEE, 1995), vol. 3, pp. 3149–3154.
12. W. McMahan, V. Chitrakaran, M. Csencsits, D. Dawson, I. D. Walker, B. A. Jones, M. Pritts, D. Dienno, M. Grissom, C. D. Rahn, Field trials and testing of the OctArm continuum manipulator, in *Proceedings 2006 IEEE International Conference on Robotics and Automation, 2006. ICRA 2006.* (IEEE, 2006), pp. 2336–2341.
13. M. Cianchetti, M. Follador, B. Mazzolai, P. Dario, C. Laschi, Design and development of a soft robotic octopus arm exploiting embodied intelligence, in *2012 IEEE International Conference on Robotics and Automation* (IEEE, 2012), pp. 5271–5276.
14. J. S. Pettinato, H. E. Stephanou, Manipulability and stability of a tentacle based robot manipulator, in *1989 IEEE International Conference on Robotics and Automation* (IEEE, 1989), pp. 458–463.
15. Z. Han, Z. Liu, W. He, G. Li, Distributed parameter modeling and boundary control of an octopus tentacle-inspired soft robot. *IEEE Trans. Control. Syst. Technol.* **30**, 1244–1256 (2022).
16. A. K. Schulz, M. Boyle, C. Boyle, S. Sordilla, C. Rincon, S. Hooper, C. Aubuchon, J. S. Reidenberg, C. Higgins, D. L. Hu, Skin wrinkles and folds enable asymmetric stretch in the elephant trunk. *Proc. Natl. Acad. Sci. U.S.A.* **119**, e2122563119 (2022).
17. A. Shikari, H. Asada, Triple scissor extender robot arm: A solution to the last one foot problem of manipulation. *IEEE Robot. Autom. Lett.* **3**, 3975–3982 (2018).
18. M. Calisti, M. Giorelli, G. Levy, B. Mazzolai, B. Hochner, C. Laschi, P. Dario, An octopus-bioinspired solution to movement and manipulation for soft robots. *Bioinspir. Biomim.* **6**, 036002 (2011).
19. R. V. Martinez, J. L. Branch, C. R. Fish, L. Jin, R. F. Shepherd, R. M. D. Nunes, Z. Suo, G. M. Whitesides, Robotic tentacles with three-dimensional mobility based on flexible elastomers. *Adv. Mater.* **25**, 205–212 (2013).
20. N. Tan, X. Gu, H. Ren, Design, characterization and applications of a novel soft actuator driven by flexible shafts. *Mech. Mach. Theory.* **122**, 197–218 (2018).
21. T. Kim, P. Kaarthik, R. L. Truby, A flexible, architected soft robotic actuator for motorized extensional motion. *Adv. Intell. Syst.* **6**, 2300566 (2024).
22. F. Connolly, C. J. Walsh, K. Bertoldi, Automatic design of fiber-reinforced soft actuators for trajectory matching. *Proc. Natl. Acad. Sci. U.S.A.* **114**, 51–56 (2017).
23. J. Bishop-Moser, S. Kota, Design and modeling of generalized fiber-reinforced pneumatic soft actuators. *IEEE Trans. Robot.* **31**, 536–545 (2015).
24. J. Yan, X. Zhang, B. Xu, J. Zhao, A new spiral-type inflatable pure torsional soft actuator. *Soft Robot.* **5**, 527–540 (2018).
25. L. H. Blumenschein, N. S. Usevitch, B. H. Do, E. W. Hawkes, A. M. Okamura, Helical actuation on a soft inflated robot body, in *2018 IEEE International Conference on Soft Robotics (RoboSoft)* (IEEE, 2018), pp. 245–252.
26. N. Oh, J.-G. Lee, H. Rodrigue, Torsional pneumatic actuator based on pre-twisted pneumatic tubes for soft robotic manipulators. *IEEE/ASME T. Mechatron.* **28**, 3191–3201 (2023).
27. D. Yang, B. Mosadegh, A. Ainla, B. Lee, F. Khashai, Z. Suo, K. Bertoldi, G. M. Whitesides, Buckling of elastomeric beams enables actuation of soft machines. *Adv. Mater.* **27**, 6323–6327 (2015).
28. Z. Jiao, C. Ji, J. Zou, H. Yang, M. Pan, Vacuum-powered soft pneumatic twisting actuators to empower new capabilities for soft robots. *Adv. Mater. Technol.* **4**, 1800429 (2019).
29. F. Chen, Y. Miao, G. Gu, X. Zhu, Soft twisting pneumatic actuators enabled by freeform surface design. *IEEE Robot. Autom. Lett.* **6**, 5253–5260 (2021).
30. T. Liu, Y. Wang, K. Lee, Three-dimensional printable origami twisted tower: Design, fabrication, and robot embodiment. *IEEE Robot. Autom. Lett.* **3**, 116–123 (2018).
31. D. Li, D. Fan, R. Zhu, Q. Lei, Y. Liao, X. Yang, Y. Pan, Z. Wang, Y. Wu, S. Liu, H. Wang, Origami-inspired soft twisting actuator. *Soft Robot.* **10**, 395–409 (2023).
32. J. I. Lipton, R. MacCurdy, Z. Manchester, L. Chin, D. Cellucci, D. Rus, Handedness in shearing auxetics creates rigid and compliant structures. *Science* **360**, 632–635 (2018).
33. L. Chin, J. Lipton, R. MacCurdy, J. Romanishin, C. Sharma, D. Rus, Compliant electric actuators based on handed shearing auxetics, in *2018 IEEE International Conference on Soft Robotics (RoboSoft)* (IEEE, 2018), pp. 100–107.
34. S. A. Etnier, Twisting and bending of biological beams: Distribution of biological beams in a stiffness mechanospace. *Biol. Bull.* **205**, 36–46 (2003).
35. S. Wolff-Vorbeck, M. Langer, O. Speck, T. Speck, P. Dondl, Twist-to-bend ratio: An important selective factor for many rod-shaped biological structures. *Sci. Rep.* **9**, 17182 (2019).
36. S. Wolff-Vorbeck, O. Speck, M. Langer, T. Speck, P. W. Dondl, Charting the twist-to-bend ratio of plant axes. *J. R. Soc. Interface* **19**, 20220131 (2022).
37. K. Bertoldi, V. Vitelli, J. Christensen, M. van Hecke, Flexible mechanical metamaterials. *Nat. Rev. Mater.* **2**, 17066 (2017).
38. J. B. Berger, H. N. G. Wadley, R. M. McMeeking, Mechanical metamaterials at the theoretical limit of isotropic elastic stiffness. *Nature* **543**, 533–537 (2017).
39. J. H. Conway, D. H. Huson, The orbifold notation for two-dimensional groups. *Struct. Chem.* **13**, 247–257 (2002).
40. J. H. Conway, H. Burgiel, C. Goodman-Strauss, *The Symmetries of Things* (CRC Press, 2016).
41. G. A. Naselli, R. B. N. Scharff, M. Thielen, F. Visentin, T. Speck, B. Mazzolai, A soft continuum robotic arm with a climbing plant-inspired adaptive behavior for minimal sensing, actuation, and control effort. *Adv. Intell. Syst.* **6**, 2300537 (2023).
42. T. G. Thuruthel, B. Shih, C. Laschi, M. T. Tolley, Soft robot perception using embedded soft sensors and recurrent neural networks. *Sci. Robot.* **4**, eaav1488 (2019).

Acknowledgments
Funding: This work was funded by the National Science Foundation grant number 2212049, a grant from the Murdock Charitable Trust, and the Office of Naval Research grant number 304220. **Author contributions:** M.C. and J.I.L. designed the cell. M.C., J.F.K., and J.G. designed the robot. M.C., J.F.K., A.G., and D.R. modeled the robot. M.C., J.F.K., J.G., and J.F.A. tested the cell. M.C., J.F.K., J.G., and J.F.A. tested the robot. M.C., J.F.K., J.F.A., D.R., and J.I.L. wrote the paper. J.I.L. provided the funding. **Competing interests:** J.I.L has filed a patent: US Patent application no. 17/759,826. **Data and materials availability:** All data and source code are publicly available at https://github.com/TransformativeRoboticsLab/TRUNC. The data are also accessible at https://doi.org/10.5281/zenodo.14962992.

Submitted 26 July 2024
Accepted 19 February 2025
Published 19 March 2025
10.1126/scirobotics.ads0548

Science Robotics

Bridging hard and soft: Mechanical metamaterials enable rigid torque transmission in soft robots

Molly Carton, Jakub F. Kowalewski, Jiani Guo, Jacob F. Alpert, Aman Garg, Daniel Revier, and Jeffrey Ian Lipton

Sci. Robot. **10** (100), eads0548. DOI: 10.1126/scirobotics.ads0548

Science Robotics (ISSN 2470-9476) is published by the American Association for the Advancement of Science. 1200 New York Avenue NW, Washington, DC 20005. The title *Science Robotics* is a registered trademark of AAAS.